

Photoacoustic cell on silicon for mid-infrared QCL-based spectroscopic analysis

Jean-Guillaume Coutard*^a, Alain Glière^a, Jean-Marc Fedeli^a, Olivier Lartigue^a, Jules Skubich^a, Guillaume Aoust^b, Alexandre Teulle^a, Thomas Strahl^c, Sergio Nicoletti^a, Mathieu Carras^b, Laurent Duraffourg^a.

^aUniv. Grenoble Alpes, CEA, LETI, MINATEC Campus, 38054 Grenoble, FRANCE; ^bmirSense, 91120 Palaiseau, FRANCE; ^cFraunhofer-Institut für Physikalische Messtechnik (IPM), 79110 Freiburg, GERMANY

ABSTRACT

Photoacoustic (PA) spectroscopy is among the most sensitive techniques used to monitor chemical emission or detect gas traces. In the mid-infrared, where most of gases of interest have their strongest absorption lines, this technique takes advantage of the high optical power and room temperature operation of quantum cascade lasers (QCL). We have recently demonstrated that centimeter-size PA cells can compete, with bulky commercial systems for gas sensing without any compromises on performances. We demonstrate a new step towards cost reduction, extreme integration, and mass deployment of such PA sensors with a miniaturized silicon PA-cell fabricated on standard CMOS tools.

The design, fabrication and characterizations of this new sub-centimeter PA cell built on a silicon platform are presented. First, the component has been designed using a detailed physical model, accounting for viscous and thermal losses, and metamodel-based optimization techniques. Second, it has been fabricated on our 200 mm CMOS pilot line. Several wafers have been released and diced. Single chips have then been assembled with commercial capacitive microphones and finally characterized on our reference gas bench. The photoacoustic simulations and the acoustics experiments are in a good agreement. The tiny PA cell exhibits a sensitivity down to the ppm level for CO₂ at 2300 cm⁻¹, as well as for CH₄ at 3057 cm⁻¹ even in a gas flow. Taking advantage of the integration of QCLs on Si and photonic circuitry, the silicon PA cell concept is currently being extended towards a fully integrated multigas detector.

Keywords: Miniaturized gas sensor, QCL, MIR, Silicon, CMOS pilot line

1. INTRODUCTION

Since the use of canaries in mines at the beginning of the 20th century, gas measurement techniques have been widely developed in a large number of activity sectors such as transport, industry, safety, etc. Among the most widespread applications, in line with current concerns, we can cite indoor air monitoring, greenhouse gas monitoring and industrial process monitoring.

Many detection methods have been used to meet the application requirements. They can be classified into two main families: based on variations in electrical property or on other types of variations¹. In the first category, we can mention solid state sensors, like MOS (metal oxide semiconductor), or polymers based sensors. In the second the optical, acoustic and chromatographic methods. Among the optical methods, the subcategories multiply with the use of schemes such as OFCEAS, TDLAS, NDIR².

In this paper, the focus is placed on the technique of photoacoustic spectroscopy. Long after the discovery of the photoacoustic effect by Graham Bell in 1880, this technique was revived in the 1970s with the availability of laser sources and has since spread widely. When applied to gas detection, it achieves performance levels that allow to reach gas trace detection, i.e. much lower than the part per million (ppm)³.

*jean-guillaume.coutard@cea.fr; phone 33 4 38 78 55 53; www.leti.fr

From the 2000s, different teams⁴ proposed to replace transduction by microphones with quartz (QEPAS) or cantilever (CEPAS)⁵ and achieved performances comparable to conventional photoacoustic approaches.

The principle of PA spectroscopy (Figure 1) relies on the excitation of a molecule of interest with a light source emitting at the wavelength of an absorption line of the molecule. The light source is modulated at the acoustic resonance frequency of a chamber containing the gas mixture. During the molecules relaxation process, kinetic energy exchange creates local periodic variations of the temperature, and thus stationary pressure waves that can be detected by high performance microphones⁶. The intensity of the signal measured by the microphone can be expressed by the following formula:

$$S_{PA} = \frac{(\gamma - 1)LQ}{\omega V_C} R_M P_0 \alpha \quad (1)$$

In this equation, γ is the Laplace coefficient, L the path length through the gas, Q the resonant cell quality factor, R_M the microphone sensitivity, P_0 the optical power of the light source, α the absorption coefficient at a wavelength for a specific gas concentration, ω the frequency and V_C the cell volume. The signal amplitude depends on the interaction path between the light source and the gas but also on the choice of the microphone, the optical power of the source and the selected of the molecule absorption line. It is worth to note that the PA signal is inversely proportional to the cell volume, which makes this type of detectors suitable for miniaturization. Usually, the signal is demodulated with a synchronous detection at the resonance frequency of the cell.

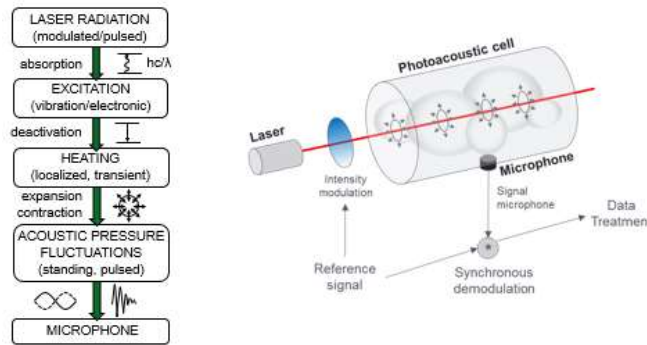


Figure 1. The principle of photoacoustic spectroscopy.

These last years, the development of the PA methods have undeniably been accelerated through the apparition of commercial, robust and powerful QCLs. These lasers emit light between 4 μm and 11 μm (Figure 2) and allow to address a number of chemical species (chemical footprint) of interest on the fundamental resonance, thus generating the most intense responses.

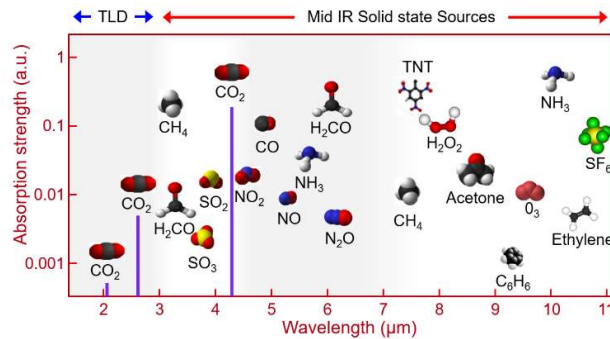


Figure 2. Gas of interest in Mid-infrared (MIR) region.

In addition, the emission bandwidth of around 0.01 cm^{-1} are narrow enough to be intrinsically selective to a specific species. On the other hand, multi-gas detection therefore requires more than one laser source or tunable lasers. Therefore, the combination of MIR and photoacoustic technologies have obvious advantages in terms of performance and have already been widely studied^{7,8}

However, commercial systems remain bulky and expensive and do not allow addressing mass markets by combining low cost and high performance.

This issue can be overcome by our approach aiming at offering these technologies integrated on silicon. The advantages the integration on planar substrate within IC/MEMS manufacturing facility is that MEMS, integrated photonic and integrated fluidic technologies can be combined together. Our ultimate goal is to propose a fully integrated monolithic system from the QCL source to the photoacoustic cell.

This approach being particularly disruptive, we first split the development of function blocks: the integration of QCLs on Si, the development MIR passive functions like for example AWG to combine the output of different sources, and the PA cell. This paper will focus on this last building block.

We studied the principle of miniaturization on a differential cell⁹ using numerical models including viscous and thermal losses¹⁰. These models were then compared experimentally using PA cells made in 3D metal prototyping termed hereafter miniPA equipped with commercial MEMS microphones glued on the cell. Under laboratory conditions (i. e. atmospheric pressure and ambient temperature), we were then able to study the behavior of these devices as gas sensors.

Tables^{11,12} allow the performance, noise and precision, of different detection technique to be evaluated. In particular by comparing the Normalized Noise Equivalent Absorption (NNEA) and the Normalized Equivalent Concentration (NEC). The NNEA coefficient measured is expressed in $\text{cm}^{-1} \cdot \text{W} \cdot \text{Hz}^{-1/2}$, by normalizing the noise equivalent absorption to a 1 Hz measurement bandwidth. We define the NEC as the gas target concentration giving a signal equal to the standard deviation value of signal intensity variations (1σ) for 1 s integration time with the available laser power. The Table 1 summarizes the results obtained with the 3D printed miniPA.

Table 1. Studied gas with miniPA 3D printed

| Gas | Optical power (mW) | Wavenumber (cm-1) | NNEA ($\text{cm}^{-1} \cdot \text{W} \cdot \text{Hz}^{-1/2}$) | NEC 1σ (ppm) |
|--|--------------------|-------------------|---|---------------------|
| CH ₄ (N ₂) | 2.2 | 2939 | $1,3 \cdot 10^{-8}$ | 0,3 |
| CO ₂ (N ₂) | 5 | 2302,5 | $1,7 \cdot 10^{-8}$ | 0,16 |
| CO(N ₂ / H ₂) | 30 | 2127 | $7 \cdot 10^{-7}$ | 0,15 |
| NO(N ₂) | 130 | 1906,1 | $3,2 \cdot 10^{-8}$ | 0,015 |
| CH ₂ O(N ₂) | 80 | 1764,95 | $2,2 \cdot 10^{-8}$ | 0,07 |
| C ₂ H ₄ O(N ₂) | 60 | 1764,95 | $1,6 \cdot 10^{-7}$ | 1 |
| C ₇ H ₈ (N ₂) | 11 | 1032 | $2,2 \cdot 10^{-8}$ | 14 |

The cell with a volume of 34 mm^3 exhibits state-of-the-art performances that already make it possible to consider the use of this device of a reliable and useful detector for many current applications. Once this proof of concept has been reached, we decided to go further in terms of miniaturization and manufacturing methods.

2. MODELLING

As mentioned, the architecture of the miniaturized silicon photoacoustic cell is based on the differential Helmholtz resonator, initially proposed by Zeninari et al⁹, and previously implemented in a steel cell produced by additive manufacturing. The layout has been adapted in order to match the constraints of MEMS microfabrication techniques, such as for instance vertical etching in planar silicon substrates and limited depth/width aspect ratio. The cell symmetrical

structure is composed of two chambers linked by capillaries (Figure 3). Gas inlet and outlet are connected in the middle of the capillaries. Although only one chamber is illuminated by a laser beam, the acoustic waves, opposite in phase at the Helmholtz resonance frequency, are generated in both chambers. The output signal consists in the difference of the measurements provided by two microphones, each sensing the pressure in one chamber.

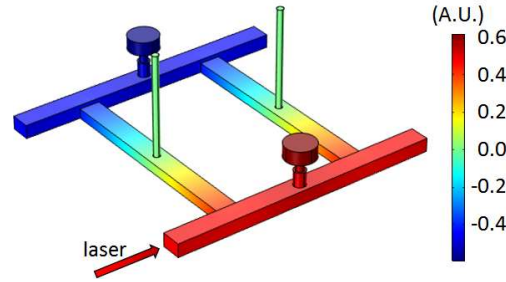


Figure 3. Geometry of the miniaturized PA cell. The pressure field at the Helmholtz resonance frequency is pictured.

2.1 Acoustic model

The acoustic model used for the design of the miniaturized cells has already been presented elsewhere and only the main information is reminded in this paper. The calculations are based on the resolution of the harmonic version of the Full Linearized Navier-Stokes (FLNS) coupled System, composed of the linearized versions of the momentum, mass and energy conservation equations. Unlike the simplified acoustic wave equation, this framework allows handling losses of viscous or thermal origin. Indeed, in the useful 5-20 kHz acoustic frequency range of interest to us, dissipative phenomena cannot be neglected because the viscous and thermal boundary layers, spanning on several tens of micrometers in air, occupy a significant proportion of the volume of the narrowest components of the acoustic network composing the photoacoustic cell.

The resolution is performed, by the finite element method, with the commercial software COMSOL Multiphysics (Comsol AB, Stockholm, Sweden). The finite element mesh of the study domain is refined in the vicinity of the walls so that several elements, usually three, are placed across the thickness of the boundary layer. Regarding boundary conditions, with the exception of microphone membranes, which are subject to a special treatment described in the next paragraph, all silicon walls are considered rigid and isothermal. The gas inlets are subject to atmospheric pressure and are not the site of any heat exchange.

The microphone model is inspired from the work of Dehe et al., who proposed a MEMS microphone equivalent electric model¹². Each part of the microphone, namely the input port, the front volume, the membrane, etched with small ventilation holes, and the back volume, is modelled by lumped electric components. This compact model (Figure 4, left) has been adapted to be easily plugged into the finite element calculation: two cylinders define the geometries of the acoustic port and front volume, while the membrane and back volume electric analogs (inductor, resistor or capacitor) are condensed into a single wall impedance Z , linking the average pressure on the membrane \bar{p} and the total volume flow I (Figure 4, right). The values of the model parameters were adjusted in order to match the response of the AKU340 microphone (Akustika, Bosch, Stuttgart, Germany), similar to the one mounted on our sensor (Figure 5).

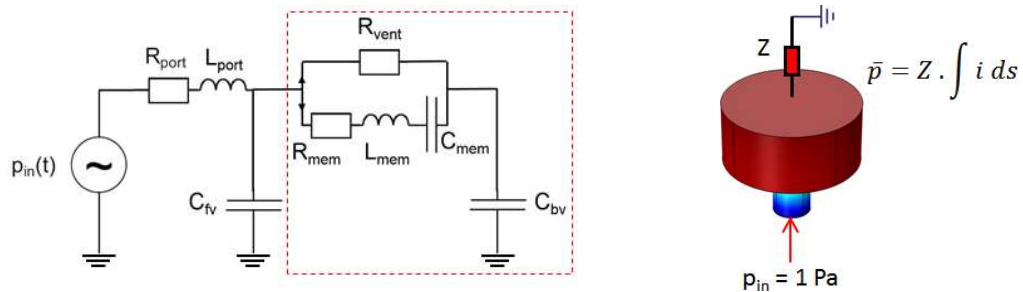


Figure 4. Compact model of the capacitive MEMS microphone (left) and its adaptation to finite element computation (right). All inductor, resistor or capacitor components enclosed in the dashed rectangle are lumped into a single wall impedance, used in the finite element model.

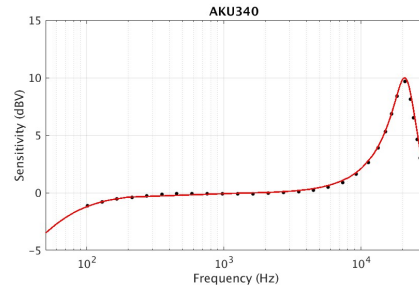


Figure 5. Acoustic response of the AKU340 microphone. Finite element calculation (solid line) overlaid with points recovered from the datasheet.

2.2 Metamodeling based design optimization

Resource intensive simulations, such as the resolution of the FLNS system by the finite element method, can hardly be used directly within an optimization algorithm, which requires multiple evaluations of the "black-box" simulator. Under these conditions, it is more effective to resort to the use of a metamodel. The process of metamodeling successively implies evaluating the numerical model response at points carefully chosen in the input parameter space (design of experiment) and then training the metamodel on the obtained dataset. Once the metamodel is built, the response at a new evaluation point can be predicted instantaneously and the metamodel can thus be used, as a surrogate of the expensive simulator, in costly procedures such as inversion or optimization.

Kriging metamodels, based on the theory of Gaussian processes, and known for their efficiency and adaptability, have been used in this work¹³. In addition, the efficient global optimization (EGO) adaptive algorithm, that improves the accuracy of the metamodel during the course of the optimization by adding new points to the initial design of experiment, has been harnessed¹³.

The design optimization has been posed as a constrained optimization problem: find the set of geometrical parameters maximizing the differential signal while keeping the cell resonance frequency under a given value. The length of the chamber, which governs the overall size of the photoacoustic cell, as well as the cross-section of the chamber, which is imposed by the angular divergence and location of the laser source, are fixed *a priori* by the designer. Only four dimensions are thus left in the parameter space, namely spacing between the chambers and between the capillaries, height and width of the capillaries.

The free software SBDO toolbox, available at [//github.com/freeSBDO/SBDOT](https://github.com/freeSBDO/SBDOT), allowed an easy implementation of the constrained optimization problem in MATLAB (The MathWorks Inc., Natick, U.S.A.).

Four configurations, corresponding to different chamber lengths (5 mm and 8 mm) and resonance frequencies (10 kHz and 15 kHz) have been optimized. With a footprint about ten times smaller (Figure 6, left) than that of the previous generation cell, made in steel by additive manufacturing¹⁴, the four novel silicon cell produce a signal of equivalent amplitude, while still respecting the resonance frequency constraints related to the relaxation time of the molecules of the gas of interest (Figure 6, right).

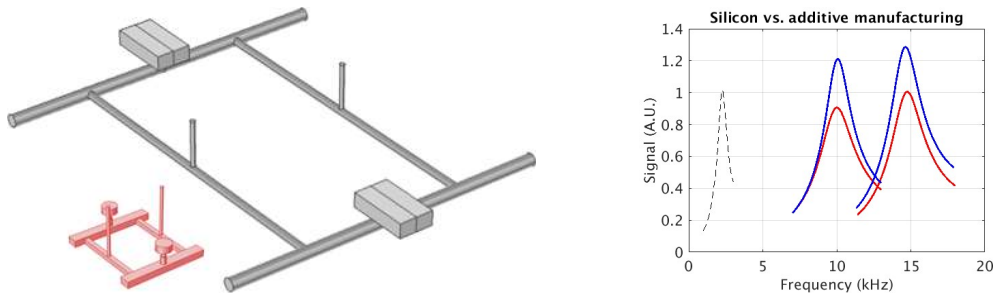


Figure 6. Footprint (left) and frequency response (right) for comparison of the previous generation steel cell and of the novel silicon cells. Computed differential signal from the steel cell (black), the small footprint (red) and larger footprint (red) silicon cells.

3. FABRICATION

The goal was to fabricate prototypes of PA cells within a 200 mm IC/MEMS technological facility. The architecture of the PA cell kept the differential approach. Therefore, based on the result of the simulation, the key points consisted in the definition of deep trenches in the silicon wafers and in the bonding of wafers.

On the upper wafer, the commercial MEMS microphone AKU350 (Akustika, Bosch Germany) was soldered and side contacts were defined. After a final dicing, the chips can be tested with ambient air or with specific gases with the introduction of thin capillaries inside the gas inlets.

4. SIGNAL CONDITIONING: DEDICATED VERY LOW-NOISE ELECTRONICS AND SIGNAL CONSIDERATIONS.

We have chosen to use commercial analog MEMS microphones from applications such as mobile phones. We chose analog devices for simplicity reason. In the case of laboratory use, they can be directly used on modular instrumentation to speed up their implementation. Digital components can also be used without any performance degradation. Instead, such microphones may be more relevant in final applications.. These devices will probably be more relevant for future integration. Indeed, they include a dedicated noise filter and signal gain algorithms that make the system more efficient. They also allow a direct link to chip or ADCs.

As every measurement systems, photoacoustic devices and sensors need to be integrated into a dedicated hardware set. However, “acoustics” does not mean that the output signal produced by the device (implying the silicon MiniPA) should be processed as an audio one.

Where many of the measurement system focus onto the quality of a whole range of frequencies or signal behavior, the selectivity of the photoacoustic working frequency involve precise considerations. Indeed, applying a classic filtering solution is interesting if many frequencies are involved but here, only one frequency is useful as we seek to gather the molecules excitation amplitude at the modulation frequency. As a result, a synchronous detection scheme is sufficient to extract the signal of interest with a lock-in amplifier. However, we have to consider the capacitive bridge effect that may drastically degrade the signal to background ratio if the microphones are directly connected to an instrument or any electronics (oscilloscope, Analog to Digital Converter ADC...). A dedicated detection chain has been implemented as shown in Figure 7. A buffer is added between the microphone and the lock-in amplifier. A specific design of this buffer has been achieved to keep the signal to noise ratio as high as possible. The buffer is made with as few components as possible to minimize the additional electronics noise..

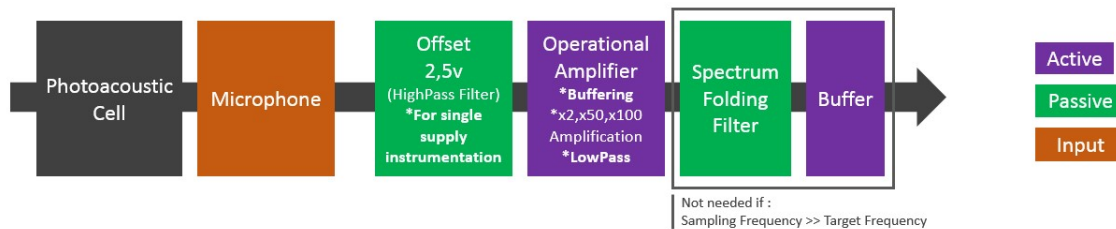


Figure 7. Dedicated instrumentation chain, for R&D testing

Furthermore, the output impedance of the used microphone is highly variable between the brands. For example, some microphone output impedances are around 100 Ω, and could be read without any major problems by some ADCs (if the filtering and the offset are managed by the device). But others have up to 1 kΩ, and a buffer is highly suitable.

Assuming that there is no correlation between the noise sources, the total noise density is the quadratic sum of the all noise densities:

$$Total\ Noise = \sqrt{Cell\ N^2 + Microphone\ N^2 + OPA\ N^2 + Filter\ N^2 + CommonMode\ N^2 + SpectrumAliasing\ N^2} \quad (2)$$

Where N is the noise amount of each block. This equation has to be minimized in particular around the resonance.

4.1 Operational amplifiers (OPA) resistors

The total amount of noise generated by the OPA is mainly produced by the resistors interacting with it. The "Gain stage" resistor multiplies the white noise from the OPA by the value of the desired gain. This noise contribution could not be reduced as it is a part of the cluster ($\text{gain} * (\text{signal} + \text{noise})$). On the other hand, the "source" resistor is also responsible of the OPA noise rising but could easily be modified. This source resistor is the load in front of the OPA which is here the resistor involved for the signal offsetting. Reducing the value of this resistor is the best way to reduce de noise but it also raise the shift of the sensor value. Indeed, when the signal goes through the capacitor, the equivalent schematic is a divider bridge. The useful signal will consequently be reduced by the ratio $R_{\text{source}} / (Z_{\text{Mic}} + R_{\text{source}})$, before being raised up $\text{Signal} + 2.5V$ (Figure 8)

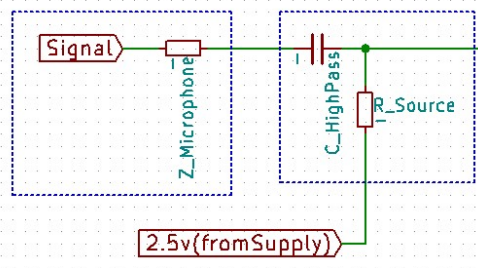


Figure 8. Divider Bridge between the Microphone and the (Optional) Offset Filter

4.2 Spectrum Aliasing

Once the signal is at the right impedance and the right amplitude, the dedicated digitalization following the system could, also, add noise by folding the frequency spectrum. A low pass filter at maximum sampling Frequency divided by two is recommended at the most important order possible. As explained previously, an 8th order Chebyshev analog filter is not suitable because the amount of OPA and Resistors will add an amount of wide band noise that will probably drown the signal into the noise. The solution is to dispatch the low pass filtering at the right place: low pass capacitor in parallel of a gain OPA block is a good solution.

4.3 Common Mode Rejection Rate/Power Supply Rejection Rate (CMRR/PSRR)

The other important way to reduce the noise is to consider the CMRR/PSRR contribution. As the microphone is supplied with the same source as all the other stages (AOPs, offsets, etc...), the more one reduce the contribution of the common mode noise, the more one protect the signal from global, low frequency, perturbations ($\text{CMRR} > 95 \text{ dB}$ under 100 Hz for the current design). Considering that the supply regulation chip are often noisy, the differential behavior of the whole supply chain is a good way to get rid of this, without being forced to filter it with heavy design (Figure 9).

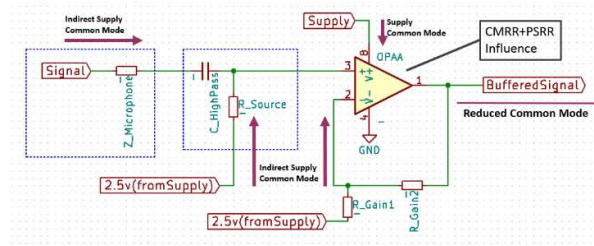


Figure 9. Common Mode behavior at the first stage of buffering

Simulation tools are a good way to explore quickly the different solutions. Especially when we need to find the right resistor value or, the right filter. Using LTspice simulation software (Analog Device, USA) this allow us achieve an ADC resolution up to 24 Bits (with the right algorithms), which help the lock-in detection to reach a very low LOD.

Finally after these optimizations steps the dedicated electronic exhibits a noise of $300 \text{ nV} \cdot \text{Hz}^{-1/2}$ around the resonance frequencies.

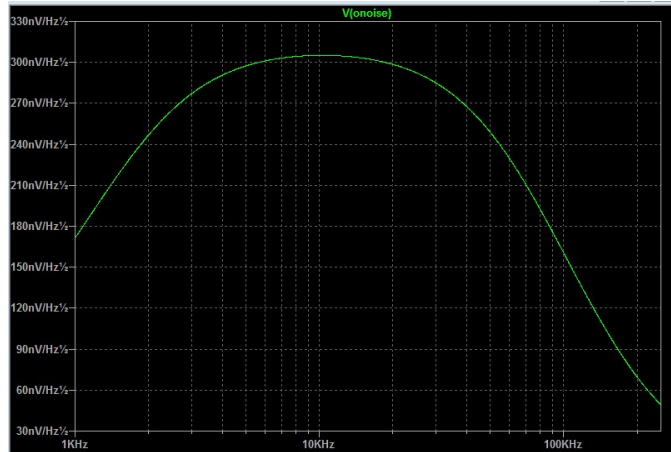


Figure 10. Noise Spectrum Distribution for the MiniPA dedicated (ProPS2) design @GAIN = x100

5. EXPERIMENTAL SETUP

We have conducted measurement tests on carbon dioxide and methane. First, using ambient CO₂ concentration, the frequency response of different versions of our cell was compared with the results obtained with the model. In a second step, using methane, we tested the linearity and detection limit. In both cases these tests were achieved using gas diffusion regime, without using a pumping system.

5.1 CO₂ detection

A continuous-wave distributed feedback Quantum Cascade Laser (DFB-QCL) on a HHL package from mirSense (Palaiseau, France) operating around $\lambda = 4.3 \mu\text{m}$ was used and an intermediate lens ensures the beam injection into the PA cell. This laser is driven in current through the LDC-3232 laser controller (Newport, USA) and the thermoelectric cooler is drive by a Newport controller. At the temperature of 14°C the tuning range of the DFB-QCL was 2 cm⁻¹ around 2302 cm⁻¹ at a mean optical power of 5.5 mW. A lock in detection SR830 (Princeton instrument, USA) is used to generate the sinusoidal signal which is injected in the laser controller to modulate the laser wavelength and to retrieve the photoacoustic signal. The wavelength varies across the absorption line of the CO₂ centered at 2302 cm⁻¹.

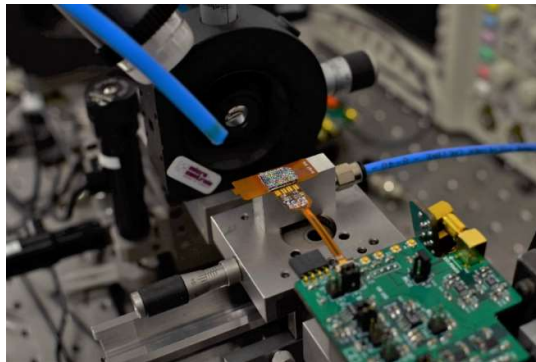


Figure 11. Diffusion setup. The Si miniPA (center) is mounted on the dedicated flexible PCB. The gas is injected via the left blue pipe.

5.2 CH₄ detection

In that case, a continuous-wave distributed feedback Interband Cascade Laser (DFB-ICL) in a TO66 mount from Nanoplus (Gerbrunn, Germany) operating at $\lambda = 3,27 \mu\text{m}$, 17°C and 43 mA was used. We used here an LDC3700 (Newport, USA) laser driver. The mean output optical power was measured at 2.5mW. The others items were the same as for the CO₂ detection.

6. RESULTS

We started by checking the frequency resonance of the different versions of the photoacoustic cells. The frequency responses are plotted in Figure 12 in differential mode. The frequency sweep was controlled through a dedicated LABVIEW (National Instruments, Austin, Texas, USA) routine. In this first measurement, a 1f-frequency detection method was used.

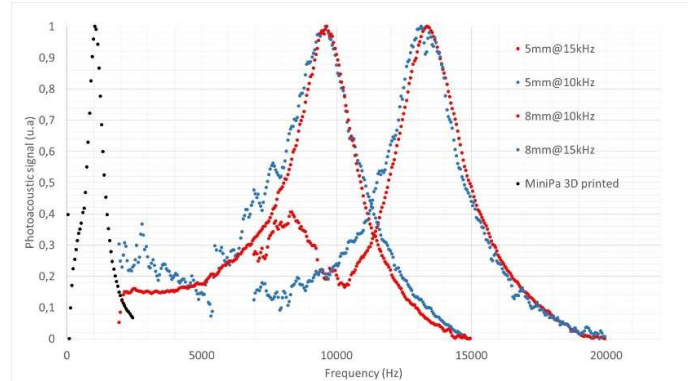


Figure 12. Resonance frequency of the silicon miniPA compared to 3D printed miniPA

In Figure 12 we note that in we obtain a very good match between the simulation (see Figure 6) and the fabrication concerning the frequency setting and the quality factor. However, for one of the curves, we observe the appearance of a secondary peak linked to a mismatch between the two chambers.

In a further measurement, we used a wavelength modulation scheme with a 2f detection strategy in order to minimize background noises¹⁵. In Figure 13 we show that the retrieved PA signal (blue dots) describe a second-derivative shape of a Lorentzian gas-absorption profile (orange dots). The maximum amplitude is directly proportional to the gas concentration. We obtained a good description of the absorption peak.

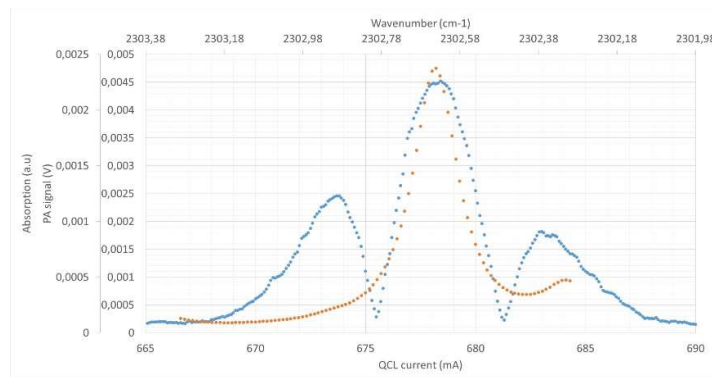


Figure 13. 2f spectroscopic measurement of CO₂ atmospheric absorption peak. A slow current ramp is applied through the peak. The integration time is set to 1 s, 12 dB/Oct. We used an 8 mm@15 kHz cell.

In the case of CH₄ detection, a calibrated gas bench was used to control the CH₄ flow rate through the cell. A typical sensitivity curve was obtained, as presented in Figure 14. The concentration was varied from 100 ppb up to 100 ppm, with a gas flow rate set at 500 mL/min. The slope is estimated around 0.05 mV/ppm with a coefficient of determination R² of 0.99.

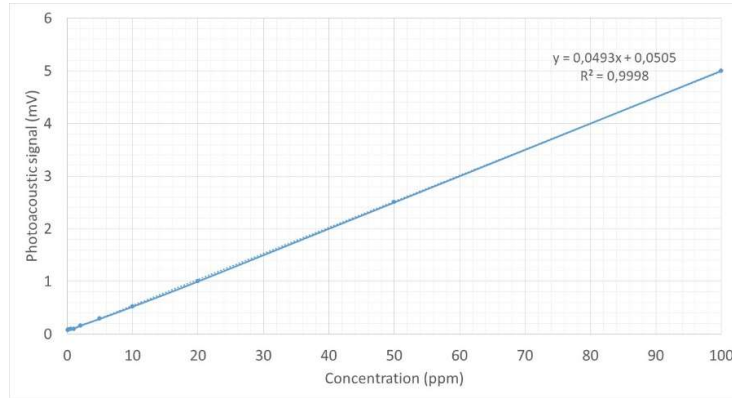


Figure 14. Concentration range of CH₄. The integration time is set to 30 ms, 6 dB/Oct.

Finally, the performance can be evaluated through the Allan deviation¹⁶, which is the image of the variation of the noise level with the integration time. The Allan deviation was measured from ambient CH₄ and the minimum detectable concentration can be extracted according to the average time as presented in Figure 15.

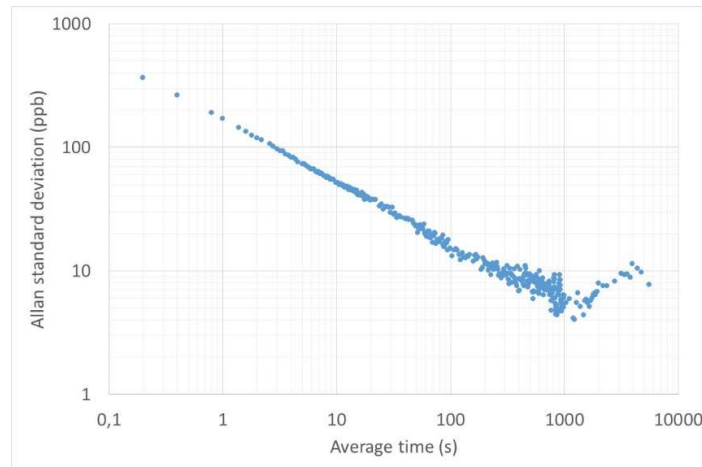


Figure 15. Allan standard deviation normalized to atmospheric methane

From the Allan deviation measurement, we can estimate the NEC and NNEA of the 8 mm@15 khz Si-cell for CH₄

$$\text{NEC} = 170 \text{ ppb (1 s)}$$

$$\text{NNEA} = 1.6 \cdot 10^{-8} \text{ cm}^{-1} \cdot \text{W} \cdot \text{Hz}^{-1/2}$$

We obtained performances in the same order of magnitude (see Table 1) than with our 3D printed miniPA with a footprint almost divide by 10.

7. CONCLUSION

We have demonstrated here the realization of an integrated photoacoustic gas sensor on silicon that are capable to measure gas trace. This miniaturized sensor makes high-resolution measurements possible using a very low gas volume. In particular, it will make it possible to build a methane detector demonstrator. The low analysis volume and the demonstrated performance (limit of detection and sensitivity) will allow obtaining a very sensitive and potentially portable sensor without any pump system.

In a second step, we will of course have to extend laboratory measurements to the real world, in particular by varying environmental conditions, such as temperature. The low volume and the material used (silicon) should be an advantage.

In addition, we will have to pursue further tests under forced gas flow conditions. Silica capillaries can already be used to inject the gas into the cell at flows of a few mL/min.

Finally, the next step will be to integrate a sound pressure transduction system directly into the photoacoustic cell. Even if the current commercial MEMS microphones are very efficient, they are not specific to the intended application. For instance, they are designed to feature a large bandwidth, covering the human hearing range, which is useless in the PA spectroscopy context. In addition, the transducers are currently mounted by reflow soldering, which complicates technological operations. Integrated transduction will eliminate this problem.

REFERENCES

- [1] Liu, X., Cheng, S., Liu, H., Hu, S., Zhang, D. and Ning, H., "A Survey on Gas Sensing Technology," *Sensors* **12**(7), 9635–9665 (2012).
- [2] Hodgkinson, J. and Tatam, R. P., "Optical gas sensing: a review," *Meas. Sci. Technol.* **24**(1), 012004 (2013).
- [3] Miklós, A., Hess, P. and Bozóki, Z., "Application of acoustic resonators in photoacoustic trace gas analysis and metrology," *Rev. Sci. Instrum.* **72**(4), 1937–1955 (2001).
- [4] Patimisco, P., Scamarcio, G., Tittel, F. and Spagnolo, V., "Quartz-Enhanced Photoacoustic Spectroscopy: A Review," *Sensors* **14**(4), 6165–6206 (2014).
- [5] Tomberg, T., Vainio, M., Hieta, T. and Halonen, L., "Sub-parts-per-trillion level sensitivity in trace gas detection by cantilever-enhanced photo-acoustic spectroscopy," *Sci. Rep.* **8**(1), 1848 (2018).
- [6] Kreuzer, L. B., "1 - The Physics of Signal Generation and Detection," [Optoacoustic Spectroscopy and Detection], Y.-H. Pao, Ed., Academic Press, 1–25 (1977).
- [7] Holthoff, E., Bender, J., Pellegrino, P. and Fisher, A., "Quantum Cascade Laser-Based Photoacoustic Spectroscopy for Trace Vapor Detection and Molecular Discrimination," *Sensors* **10**(3), 1986–2002 (2010).
- [8] González, A., Pozo, J. and Nicoletti, S., "Mid-Infrared Chemical Sensors for Transport, Environment and Space," *Opt. Photonik* **12**(5), 18–19 (2017).
- [9] Zéninari, V., Kapitanov, V. A., Courtois, D. and Ponomarev, Y. N., "Design and characteristics of a differential Helmholtz resonant photoacoustic cell for infrared gas detection," *Infrared Phys. Technol.* **40**(1), 1–23 (1999).
- [10] Glière, A., Rouxel, J., Parvitte, B., Boutami, S. and Zéninari, V., "A Coupled Model for the Simulation of Miniaturized and Integrated Photoacoustic Gas Detector," *Int. J. Thermophys.* **34**(11), 2119–2135 (2013).
- [11] Elia, A., Lugarà, P. M., Di Franco, C. and Spagnolo, V., "Photoacoustic Techniques for Trace Gas Sensing Based on Semiconductor Laser Sources," *Sensors* **9**(12), 9616–9628 (2009).
- [12] Dehe, A., Wurzer, M., Fuldner, M. and Krumbein, U., "The Infineon Silicon MEMS Microphone," presented at AMA Conferences 2013, 2013, Nürnberg, Germany, May 14-16, 95–99.
- [13] Forrester, A., Sobester, D. A. and Keane, A., [Engineering Design via Surrogate Modelling: A Practical Guide], John Wiley & Sons (2008).
- [14] Rouxel, J., Coutard, J.-G., Gidon, S., Lartigue, O., Nicoletti, S., Parvitte, B., Vallon, R., Zéninari, V. and Glière, A., "Miniaturized differential Helmholtz resonators for photoacoustic trace gas detection," *Sens. Actuators B Chem.* **236**, 1104–1110 (2016).
- [15] Cassidy, D. T. and Reid, J., "Harmonic detection with tunable diode lasers —two-tone modulation," *Appl. Phys. B* **29**(4), 279–285 (1982).
- [16] T. J. Witt, "Using the Allan variance and power spectral density to characterize DC nanovoltmeters," in *IEEE Transactions on Instrumentation and Measurement*, vol. 50, no. 2, pp. 445-448 (2001).

ACKNOWLEDGEMENTS

This project has received funding from the European Union's Horizon 2020 research and innovation programme under grant agreement No 780240.